

OBSERVATION OF AN EXTENDED VHE GAMMA-RAY EMISSION FROM MSH 15–52 WITH CANGAROO-III

T. NAKAMORI¹ H. KUBO¹ T. YOSHIDA² T. TANIMORI¹ R. ENOMOTO³ G. V. BICKNELL⁴ R. W. CLAY⁵ P. G. EDWARDS⁶
S. GUNJI⁷ S. HARA⁸ T. HARA⁹ T. HATTORI¹⁰ S. HAYASHI¹¹ Y. HIGASHI¹ Y. HIRAI² K. INOUE⁷ S. KABUKI¹ F. KAJINO¹¹
H. KATAGIRI¹² A. KAWACHI¹⁰ T. KIFUNE³ R. KIUCHI³ J. KUSHIDA¹⁰ Y. MATSUBARA¹³ T. MIZUKAMI¹ Y. MIZUMOTO¹⁴
R. MIZUNIWA¹⁰ M. MORI³ H. MURAISHI¹⁵ Y. MURAKI¹³ T. NAITO⁹ S. NAKANO¹ D. NISHIDA¹ K. NISHIJIMA¹⁰ M. OHISHI³
Y. SAKAMOTO¹⁰ A. SEKI¹⁰ V. STAMATESCU⁵ T. SUZUKI² D. L. SWABY⁵ G. THORNTON⁵ F. TOKANAI⁷ K. TSUCHIYA¹
S. WATANABE¹ Y. YAMADA¹¹ E. YAMAZAKI¹⁰ S. YANAGITA² T. YOSHIKOSHI³ Y. YUKAWA³

Draft version August 11, 2021

ABSTRACT

We have observed the supernova remnant MSH 15–52 (G320.4–1.2), which contains the gamma-ray pulsar PSR B1509–58, using the CANGAROO-III imaging atmospheric Cherenkov telescope array from April to June in 2006. We detected gamma rays above 810 GeV at the 7 sigma level during a total effective exposure of 48.4 hours. We obtained a differential gamma-ray flux at 2.35 TeV of $(7.9 \pm 1.5_{\text{stat}} \pm 1.7_{\text{sys}}) \times 10^{-13} \text{ cm}^{-2} \text{ s}^{-1} \text{ TeV}^{-1}$ with a photon index of $2.21 \pm 0.39_{\text{stat}} \pm 0.40_{\text{sys}}$, which is compatible with that of the H.E.S.S. observation in 2004. The morphology shows extended emission compared to our Point Spread Function. We consider the plausible origin of the high energy emission based on a multi-wavelength spectral analysis and energetics arguments.

Subject headings: gamma rays:observations – ISM: individual(MSH 15–52, G320.4–1.2) – supernova remnants – pulsars: individual(PSR B1509-58)

1. INTRODUCTION

Recent imaging atmospheric Cherenkov telescopes (IACTs) have achieved remarkably high sensitivity in the very high energy gamma-ray band. This is well illustrated by the Galactic plane survey carried out by the H.E.S.S. collaboration (Aharonian et al. 2006; Hoppe 2007). Many of the discovered TeV sources are associated with pulsar wind nebulae (PWNe) (e.g., Gaensler & Slane 2006), which are now established as the most populous category among Galactic TeV sources: 18 PWNe have been found so far (Hinton 2007) and a portion of 21 unidentified galactic TeV sources could

be PWNe as well (Aharonian et al. 2007b; Funk et al. 2007b).

The Crab nebula, the prototype PWN, has been observed in every accessible wave band. The nebula contains the Crab pulsar, which has the highest spindown energy loss of known gamma-ray pulsars (Thompson 2003). However, the radiation mechanism remains controversial for the Crab nebula and for other PWNe: it has been argued that the Crab nebula’s broadband spectral energy distribution (SED) can be well explained by synchrotron emission in an average magnetic field of $\sim 0.1 - 0.3 \text{ mG}$ for radio to soft gamma-ray bands, and by inverse Compton (IC) scattering of synchrotron, IR, millimeter and cosmic microwave background (CMB) photons for the hard gamma-ray band up to 100 TeV (Aharonian & Atoyan 1996; Atoyan & Aharonian 1996; Aharonian, Atoyan & Kifune 1997; Aharonian & Atoyan 1998; Aharonian et al. 2004). On the other hand, it was claimed that gamma rays from the decay of neutral pions, produced by hadrons, contribute significantly at $\sim 10 \text{ TeV}$ for the Crab nebula (Bednarek & Bartosik 2003). Consideration has also been given to whether the energy source of TeV gamma-ray emission from an SNR containing a pulsar (composite SNR) is the pulsar’s spindown energy or related to the supernova explosion (e.g. Funk et al. 2007b), and the efficiency of energy conversion to the particle acceleration for such models.

PSR B1509–58 has the third highest spindown energy loss after the Crab pulsar (Thompson 2003) and PSR J1833-1034 (Camilo et al. 2006) in the Galaxy, and its nebula has also been well studied across the electromagnetic spectrum. TeV gamma-ray observations, combined with those at other energy bands, provide additional information which may lead to solutions for the above problems and a unified comprehension of pulsar and nebula systems. PSR B1509–58 was detected in the radio supernova remnant MSH 15–52 (G320.4–1.2)

Electronic address: nakamori@cr.scephys.kyoto-u.ac.jp

¹ Department of Physics, Kyoto University, Sakyo-ku, Kyoto 606-8502, Japan

² Faculty of Science, Ibaraki University, Mito, Ibaraki 310-8512, Japan

³ Institute for Cosmic Ray Research, University of Tokyo, Kashiwa, Chiba 277-8582, Japan

⁴ Research School of Astronomy and Astrophysics, Australian National University, ACT 2611, Australia

⁵ School of Chemistry and Physics, University of Adelaide, SA 5005, Australia

⁶ CSIRO Australia Telescope National Facility, Narrabri, NSW 2390, Australia

⁷ Department of Physics, Yamagata University, Yamagata, Yamagata 990-8560, Japan

⁸ Ibaraki Prefectural University of Health Sciences, Ami, Ibaraki 300-0394, Japan

⁹ Faculty of Management Information, Yamanashi Gakuin University, Kofu, Yamanashi 400-8575, Japan

¹⁰ Department of Physics, Tokai University, Hiratsuka, Kanagawa 259-1292, Japan

¹¹ Department of Physics, Konan University, Kobe, Hyogo 658-8501, Japan

¹² Department of Physical Science, Hiroshima University, Higashi-Hiroshima, Hiroshima 739-8526, Japan

¹³ Solar-Terrestrial Environment Laboratory, Nagoya University, Nagoya, Aichi 464-8602, Japan

¹⁴ National Astronomical Observatory of Japan, Mitaka, Tokyo 181-8588, Japan

¹⁵ School of Allied Health Sciences, Kitasato University, Sagami-hara, Kanagawa 228-8555, Japan

(Caswell et al. 1981), initially as a 150-ms X-ray pulsar with the *Einstein* satellite (Seward & Harden 1982), which was confirmed by later X-ray/soft gamma-ray observations (Kawai et al. 1993; Matz et al. 1994; Gunji et al. 1994; Saito et al. 1997; Marsden et al. 1997; Cusumano et al. 2001; Forot et al. 2006). Subsequently its pulse period was detected at radio frequencies (Manchester et al. 1982), and at soft gamma-ray energies with COMPTEL (Kuiper et al. 1999). The pulsar was detected above 30 MeV by EGRET at the 4.4σ level with some suggestive, if not statistically compelling, evidence of modulation at the pulsar period (Kuiper et al. 1999). Although optical (Shearer et al. 1998) and near-IR (Kaplan & Moon 2006) searches found possible pulsar counterparts, the pulse period was not detected. As one of the most energetic young pulsars, PSR B1509–58, has been particularly well studied at radio wavelengths. A detailed timing analysis yielded a period derivative of $\dot{P} = 1.5 \times 10^{-12}$, and a high spin-down luminosity of $\dot{E} = 1.8 \times 10^{37} I_{45} \text{ ergs s}^{-1}$, where I_{45} is the moment of inertia in units of 10^{45} g cm^2 . A braking index of $n = 2.84$ was measured, corresponding to an age, assuming an initial period of $P_0 \ll P$, of $\tau = (P/(n-1)\dot{P})[1 - (P_0/P)^{n-1}] \sim (P/(n-1)\dot{P}) \sim 1700 \text{ yr}$. A large dipole surface magnetic field of $B = 1.5 \times 10^{13} \text{ G}$ was also inferred (Kaspi et al. 1994; Livingstone et al. 2005). However, in contrast to other young pulsars, no pulsar glitch has been observed to date. Initially, the age of the SNR was estimated to be 6–20 kyr (Seward et al. 1983) or ~ 10 kyr (Van den Bergh & Kramper 1984) prompting debate about the disagreement with the pulsar’s age. Blandford & Romani (1988) and Gvaramadze (2001), for instance, suggested the pulsar age was actually ≥ 20 kyr. The latter was based on the assumption that pulsar’s braking torque was enhanced by the interaction between the pulsar’s magnetosphere and circumstellar dense clumps.

The radio morphology of MSH 15–52 consists of southeast and northwest shells. The latter, $\sim 10'$ from the pulsar, spatially coincides with the H α nebula RCW89 (Rodgers et al. 1960), and Gaensler et al. (1999) concluded that MSH 15–52, PSR B1509–58 and RCW89 were associated systems. The distance, derived from an HI absorption measurement, is $5.2 \pm 1.4 \text{ kpc}$, consistent with the value of $5.9 \pm 0.6 \text{ kpc}$ determined from the pulsar dispersion measure (Taylor & Cordes 1993). We adopt $d = 5.2 \text{ kpc}$ throughout this paper.

Symmetric jets, similar to the Crab pulsar (Brinkmann et al. 1985) and the Vela pulsar (Helfand et al. 2001), were observed by *ASCA* (Tamura et al. 1996), *ROSAT* (Trussoni et al. 1996) and *Chandra* (Gaensler et al. 2002). The jet directed towards the northwest was observed to terminate at RCW89. Precise *Chandra* observations revealed the sequential heating of the knots in RCW89 by the pulsar jet (Yatsu et al. 2005). The high resolution *Chandra* image also showed the arc structure where the pulsar wind may be terminated, and the diffuse pulsar wind nebula (Gaensler et al. 2002), which emitted non-thermal synchrotron radiation. However the PWN has not been observed at other wavelengths such as IR or optical. Although IRAS found an infrared source, *IRAS* 15099–5856, spatially coincident with PSR B1509–58,

the IR emission was thermal and therefore not related to the PWN (Arendt 1991). A faint radio structure was detected (Gaensler et al. 1999) but its flux density was obtained only within a large error (Gaensler et al. 2002). A larger extent than that of X-ray was expected due to the difference of the cooling lifetime so that it was thought to be partially hidden by the bright RCW89.

The *Ginga* LAC discovered single power-law emission up to 20 keV with a photon index of ~ 2 , indicating synchrotron emission and the existence of accelerated electrons (Asaoka & Koyama 1990). The synchrotron nebula spectrum was also measured by *EINSTEIN* (Seward et al. 1983), *EXOSAT* (Trussoni et al. 1990) and *RXTE* (Marsden et al. 1997). *BeppoSAX* detected nonthermal emission from 1 keV up to 200 keV with a photon index of $\Gamma = 2.08 \pm 0.01$ (Mineo et al. 2001), while recent observations with *INTEGRAL* IBIS found a possible (2.9σ) spectral cut off at $\sim 160 \text{ keV}$ (Forot et al. 2006). Since high energy electrons were demonstrated to exist, very high energy gamma-ray emission was predicted via IC scattering with CMB photons (du Plessis et al. 1995; Harding 1996). CANGAROO-I also suggested a possible VHE gamma-ray detection of $\sim 10\%$ of the Crab flux above 1.9 TeV, assuming a spectral photon index of 2.5 (Sako et al. 2000). H.E.S.S. subsequently reported extended VHE gamma-ray emission along with the pulsar jet. Their TeV morphology showed a good coincidence with X-ray images, indicating that the TeV gamma-rays originate from the inverse Compton scattering of relativistic electrons. It was pointed out that IC scattering of the CMB could not account for most of the TeV gamma-ray flux with an assumed magnetic field of $17 \mu\text{G}$, which indicated the contribution of IR photons as seed photons for the IC process (Aharonian et al. 2005; Khélifi et al. 2005). The necessity for target photons in addition to the CMB has recently been suggested for other Galactic sources also (Khélifi et al. 2005; Hinton & Aharonian 2007). Here we report the results of TeV gamma-ray observations with the CANGAROO-III telescopes and consider the origin of the TeV gamma-ray emission based on a discussion of the energetics.

2. CANGAROO-III OBSERVATIONS

CANGAROO-III is an array of four IACTs, located at Woomera, South Australia ($136^\circ 47' \text{E}$, $31^\circ 06' \text{S}$, 160 m a.s.l.). Each telescope has a 10 m diameter reflector which consists of 114 segmented FRP spherical mirrors mounted on a parabolic frame (Kawachi et al. 2001). The telescopes are situated at the corners of a diamond with $\sim 100 \text{ m}$ sides (Enomoto et al. 2002). The oldest telescope, T1, which was the CANGAROO-II telescope, was not used due to its smaller FOV and higher energy threshold. The imaging camera systems on the other three telescopes (T2, T3 and T4) are identical, with 427 PMTs and a FOV of 4.0° (Kabuki et al. 2003). The PMT signals were recorded by charge ADCs and multi-hit TDCs (Kubo et al. 2003). The observations were made from April to June in 2006. The tracking positions were offset by $\pm 0.5^\circ$ from PSR B1509–58 in declination or in right ascension, and changed every twenty minutes, in order to suppress position-dependent effects on the camera due to bright (4.1 and 4.5 magnitude) stars. To trigger data recording, an individual telescope

was required to have more than four pixels registering over 7.6 photoelectrons within 100 nsec (local trigger), with a global trigger system then determining the coincidence of any two of the three telescopes (Nishijima et al. 2005). We rejected data taken in bad weather conditions in which the shower event rate was less than 5 Hz or at zenith angles larger than 35° . Finally, the selected data were taken at a mean zenith angle of 30.1° with a corresponding Point Spread Function (PSF) of 0.23° (68% containment radius). A typical trigger rate of 3-fold coincidence is 12 Hz. The effective exposure time amounts to 48.4 hours.

3. DATA REDUCTION AND ANALYSIS

The basic analysis procedures are described in detail in Enomoto et al. (2006) and Kabuki et al. (2007). Using calibration data taken daily with LEDs, the recorded charges of each pixel in the camera were converted to photoelectrons. At this step we found 8 bad pixels out of 427×3 due to their higher or lower ADC conversion factors in these observations. These bad pixels were removed from this analysis period, which was also reflected in the Monte Carlo simulations. Then every shower image was cleaned through the following CANGAROO-III standard criteria. Only pixels which received ≥ 5.0 photoelectrons were used as “hit pixels”. Then five or more adjacent hit pixels, with arrival times within 30 nsec from the average hit timing of all pixels, were recognized as a shower cluster.

We carefully studied the effect of the bright stars by monitoring the mean ADC counts of the pixels for which the stars entered the FOV. When the stars were within the pixel’s FOV, the PMT hit rate increased significantly. At such times the “hits” for that pixel were dominated by the starlight triggers, which were dimmer than “hits” by air shower Cherenkov photons. The average ADC counts of the affected pixels were clearly reduced during such times. After the image cleaning procedure above, the averaged ADC counts became stable within the usual values over the whole run, indicating the effects of the stars were completely removed.

Before calculating image moments — the “Hillas parameters” (Hillas 1985) — we applied the “edge cut” described in Kabuki et al. (2007). If the brightest 15 pixels in the image (or all pixels for images with less than 15 hits) were not located in the outer edge layer of the camera, we retained the event. The orientation angles were determined by minimizing the sum of squared *widths* with a constraint given by the *distance* predicted by the Monte Carlo simulations.

Then we applied the Fisher Discriminant method (Fisher 1936; Enomoto et al. 2006) with a multi-parameter set of $\vec{P} = (W_2, W_3, W_4, L_2, L_3, L_4)$, where W and L are the energy corrected *width* and *length*, and suffixes identify the telescope. The Fisher Discriminant (FD) is defined as $FD \equiv \vec{\alpha} \cdot \vec{P}$ where $\vec{\alpha}$ is a set of coefficients mathematically determined to maximize the separation between FD for gamma-rays and hadrons.

For the background study we selected a ring region around the target, $0.2 \text{ deg}^2 \leq \theta^2 \leq 0.5 \text{ deg}^2$, and obtained FD distributions for background, F_b , and Monte Carlo gamma-rays, F_g . Finally we could fit the FD distributions of the events from the target with a linear combination of these two components. The observed FD distri-

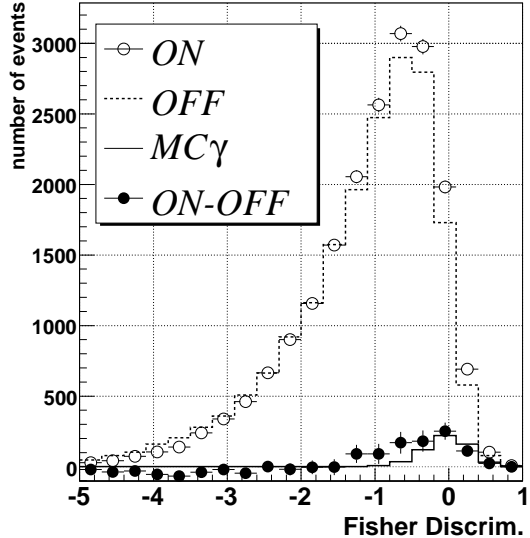


FIG. 1.— FD distribution. The open circles show the FD obtained from the ON source region, $\theta^2 < 0.1 \text{ deg}^2$. The broken and solid histogram are the background and gamma-ray component estimated by the fit procedure described in the text. The filled circles are the subtraction of the background from the ON source region.

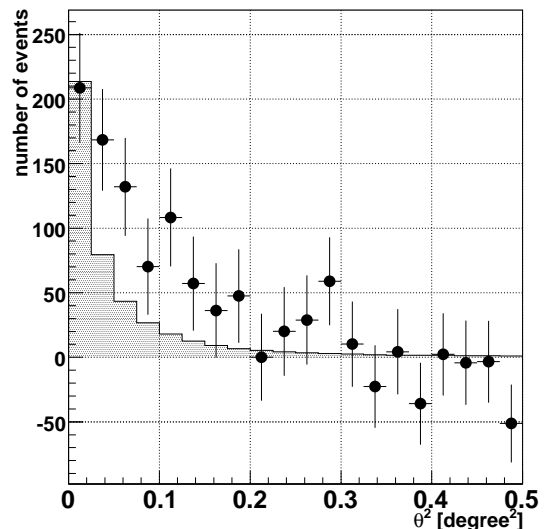


FIG. 2.— The θ^2 plot. Here, 0 deg corresponds to the best-fit position of the centroid of the emission obtained by this work (see text). The hatched histogram represents our PSF derived from the Monte-Carlo simulation.

butions, F , should be represented as $F = \alpha F_g + (1 - \alpha) F_b$ where α is the ratio of gamma-ray events to total events. Here only α is optimized and the obtained FD distributions are shown in Fig. 1. This analysis method was checked by an analysis of the Crab nebula data taken in December 2005.

The reflectivities of each telescope, which are used in the simulations, are monitored every month by a muon ring analysis of calibration run individually taken by each telescope. We obtained relative light collecting efficiencies with respect to the original mirror production time of 0.61, 0.64, and 0.67 for T2, T3 and T4, respectively.

4. RESULTS

The obtained θ^2 plot is shown in Fig. 2 with the PSF of our telescopes. Above 810 GeV we detected 427 ± 63 excess events under the assumption the TeV source was a

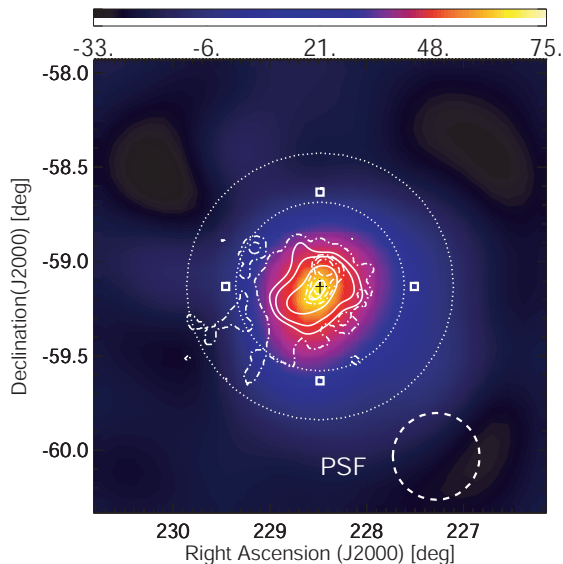


FIG. 3.— Morphology of gamma-ray like events, smoothed with a gaussian of $\sigma = 0.23^\circ$. Our PSF is also shown by a dashed circle (68% containment radius). The squares and the cross represent tracking positions and the pulsar position, respectively. Solid contours show VHE gamma-ray emission as seen by H.E.S.S. and dotted contours by *ROSAT* 0.6–2.1 keV (Trussoni et al. 1996). The region between thin dotted circles are used for the background study.

point source ($\theta^2 < 0.06 \text{ deg}^2$) and 582 ± 77 events (7.6σ) within $\theta^2 < 0.1 \text{ deg}^2$, which corresponds to the size of the SNR. The TeV gamma-ray emission is extended, and the morphology of gamma-ray-like events, smoothed by a gaussian with $\sigma = 0.23 \text{ deg}$, is shown in Fig. 3. The number of events were individually estimated by the FD-fitting method in each $0.2^\circ \times 0.2^\circ$ sky bin. When we evaluate the outer regions ($\theta^2 > 0.6 \text{ deg}^2$), we must consider the gradual deformations of the FD distributions at larger angular distances from the target. Therefore we selected a ring with radii $0.2^\circ < r < 0.4^\circ$ centered on the evaluated region as the background. For the inner regions, $\theta^2 < 0.6 \text{ deg}^2$, the same background as used in Fig. 2 was adopted. The intrinsic extent of the TeV gamma-ray emission was estimated by the 2D Gaussian fit on our unsmoothed excess map. The inclination of the major axis is $61.3 \pm 1.9^\circ$, measured to the north from west, which is compatible with the jet direction determined by *Chandra*, H.E.S.S. and *INTEGRAL*. The intrinsic source sizes along the major and minor axes were calculated to be $0.07 \pm 0.07^\circ$ and $0.21 \pm 0.08^\circ$, respectively. The center of gravity of the TeV gamma-ray emission is at (R.A., Dec.) = $(228^\circ.486, -59^\circ.235)$, which corresponds to the offset from the pulsar in (R.A., Dec.) = $(0^\circ.0030 \pm 0^\circ.0076, 0^\circ.10 \pm 0^\circ.012)$. No significant offset from the pulsar is then observed given our PSF, while the H.E.S.S. measurement showed the offset of $(0^\circ.048, 0^\circ.022)$ in (R.A., Dec.) at the 3σ level. Fig. 4 represents a reconstructed VHE gamma-ray spectrum compatible with a single power-law: the value at 2.35 TeV is $(7.9 \pm 1.5_{\text{stat}} \pm 1.7_{\text{sys}}) \times 10^{-13} \text{ cm}^{-2} \text{ s}^{-1} \text{ TeV}^{-1}$ with a photon index of $2.21 \pm 0.39_{\text{stat}} \pm 0.40_{\text{sys}}$. The flux was measured within $\theta^2 < 0.1 \text{ deg}^2$. The relevant systematic errors are due to the atmospheric transparency, NSB fluctuations, uniformity of camera pixels, and light collecting efficiencies. In addition, the signal integrating region was changed from $\theta^2 < 0.1 \text{ deg}^2$ to

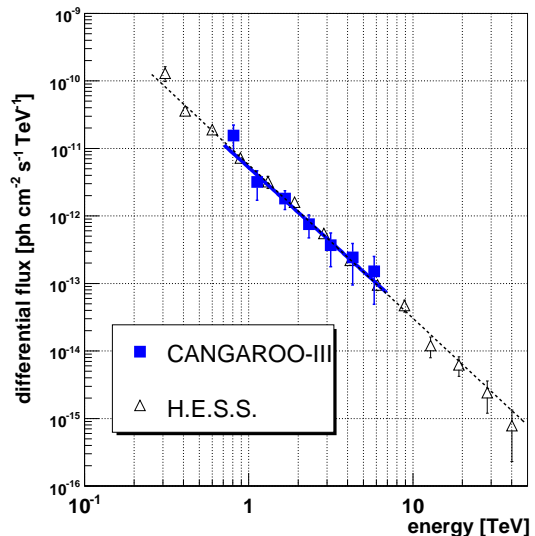


FIG. 4.— Differential flux of the whole nebula. Squares and triangles show the CANGAROO-III and the H.E.S.S. data points, respectively. The best fit power-laws are also shown by the solid and dashed line from this work and from H.E.S.S., respectively. 0.2 deg^2 in Fig. 2, which was included in the systematic error. The TeV gamma-ray extent and flux obtained by CANGAROO-III are consistent with those obtained with H.E.S.S. Our result indicates the TeV gamma-ray emission does not vary significantly between the H.E.S.S. observations in 2004 and ours in 2006, which is also consistent with the steady X-ray emission from the diffuse PWN over several decades (Delaney et al. 2006). Sako et al. (2000) reported a marginal detection (4.1σ) above 1.9 TeV of $(2.9 \pm 0.7_{\text{stat}}) \times 10^{-12} \text{ ergs cm}^2 \text{ s}^{-1}$. For the sake of comparison, we integrated the differential flux of this work over the same energy band with a photon index of 2.5 as inferred by Sako et al. (2000), and obtained $(1.6 \pm 0.4_{\text{stat}}) \times 10^{-12} \text{ ergs cm}^2 \text{ s}^{-1}$, marginally outside the 1σ error range of the CANGAROO-I result.

5. DISCUSSION

We discuss the possible origin of the TeV gamma-ray emission from the PWN for both proposed cases of its age: $\tau = 1700 \text{ yr}$ and 20 kyr (Blandford & Romani 1988; Gvaramadze 2001).

5.1. Upper limit on the global energetics

In general, two alternatives of the energy source of a composite SNR could be considered, namely the pulsar's spindown energy and the supernova explosion (or the SNR). In the latter case, the energy could be as high as $\sim 10^{51}$ ergs, or even up to a few times 10^{52} ergs for some SNe Ib/c and SNe IIn (Nomoto et al. 2001). However, in the case of MSH 15–52, the extent of the intrinsic TeV gamma-ray morphology shows a good coincidence not with the shell of MSH 15–52 but with the jet and the PWN. Therefore we rejected the scenario in which the SNR is at the origin of the high energy particles. Hereafter we assume the pulsar's spindown energy is the global energy source.

The time evolution of the pulsar period $P(t)$ is described as

$$P(t) = P_0 \left(1 + \frac{t}{\tau_0}\right)^{\frac{1}{n-1}}, \quad (1)$$

where τ_0 is a parameter called the initial spindown time

TABLE 1
 τ_0 DEPENDENCE OF PARAMETERS.

PSR	τ_0 [yr]	E_{tot} [ergs]	P_0 [msec]
B1509–58	30	7.5×10^{49}	16
	($\tau=1700$ yr)	2.1×10^{49}	31
	300	7.2×10^{48}	53
	500	4.6×10^{48}	67
	700	3.6×10^{48}	77
Crab	1000	2.8×10^{48}	87
	30 ^a	1.1×10^{51}	3.3
	700 ^b	3.7×10^{49}	19

^a Atoyan (1999) argued that the observed radio spectrum suggested $\tau_0 = 30$ yr.

^b derived from eq. (4).

scale, assuming both n and k in the braking equation $\dot{\Omega} = -k\Omega^n$ are constant (e.g., Gaensler & Slane 2006). The pulsar’s spindown energy $\dot{E}(t)$ is then calculated as

$$\dot{E}(t) = \dot{E}_0 \left(1 + \frac{t}{\tau_0}\right)^{-\alpha}, \quad \alpha = \frac{n+1}{n-1} \quad (2)$$

where \dot{E}_0 is the initial spindown luminosity. By integrating this, we obtain the total energy which the pulsar has lost over its age, τ ,

$$E_{tot} = \int_0^\tau \dot{E}(t) dt = \frac{\dot{E}_0 \tau_0}{1-\alpha} \left[\left(1 + \frac{\tau}{\tau_0}\right)^{1-\alpha} - 1 \right]. \quad (3)$$

This formula provides an upper limit to the energy supplied by the pulsar to the PWN as a function of the unknown parameter τ_0 . For the sake of simplicity, energy loss through adiabatic expansion was neglected here. The dependence of E_{tot} on τ_0 is listed in Table 1, where the pulsar’s moment of inertia was assumed to be 10^{45} g cm^2 . The value of τ_0 also determines the initial spin period P_0 , using the current period $P(\tau)$, as listed in Table 1. For comparison, the E_{tot} and P_0 for the Crab pulsar were also listed in Table 1, with $P = 33$ msec, $\dot{P} = 4.2 \times 10^{-13}$ (Taylor & Cordes 1993), $\tau = 950$ yr, $\dot{E}(\tau) = 5 \times 10^{38} \text{ ergs s}^{-1}$ and $n = 2.5$ (Lyne et al. 1988). The E_{tot} of the Crab is about 10 times larger than that of PSR B1509–58 for the same τ_0 .

For $\tau = 1700$ yr, we can calculate τ_0 as

$$\tau_0 = \frac{P(\tau)}{(n-1)\dot{P}(\tau)} - \tau \sim 30 \text{ yrs.} \quad (4)$$

However, in the $\tau = 20$ kyr case, these formulae are not applicable due to the possibility of a time-dependence for k (Blandford & Romani 1988). It is hard to estimate an accurate E_{tot} , however, a larger E_{tot} than that estimated for $\tau = 1700$ yrs would be expected.

5.2. Hadronic scenario

Hadronic gamma-ray production in PWNe has been suggested for the Crab nebula (Bednarek & Bartosik 2003; Amato et al. 2003) and the Vela X region (Bednarek 2007; Horns 2006; Horns et al. 2007). First we examine a neutral-pion decay model for the origin of the TeV gamma-ray emission. Fig. 5 shows the spectral energy distribution (SED). We assumed the population of accelerated protons to be expressed by a single power-law with an exponential cutoff, that is, $dN_p/dE_p \propto E_p^{-\gamma_p} \exp(-E_p/E_{max})$. We used only our data and the

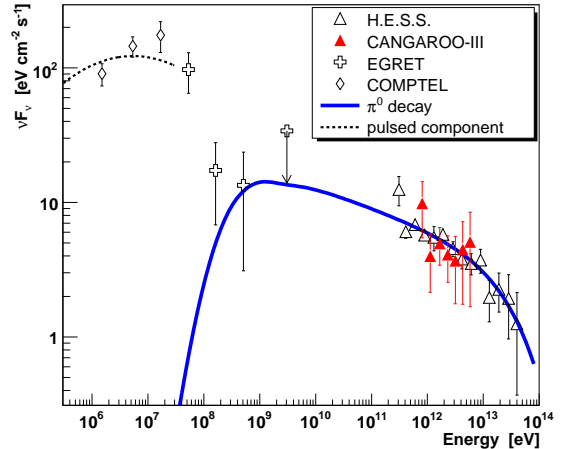


FIG. 5.— Spectral energy distribution and the model curve of neutral pion decay. The solid line represents the best fit model curve. COMPTEL and EGRET flux points were omitted from the fit since they contained pulsed emission from the pulsar. A dashed line cited from Cusumano et al. (2001) represents a model fit curve of the pulsed emission obtained by *BeppoSAX* and COMPTEL.

H.E.S.S. data (Aharonian et al. 2005) for the model fit since the COMPTEL and EGRET data were the sum of pulsed and unpulsed emission (Kuiper et al. 1999) which may contain emission from the pulsar. The contribution of the pulsed emission is indicated by the dashed line in Fig. 5, derived from a fit to the *BeppoSAX* and COMPTEL data of the pulsed emission (Cusumano et al. 2001) (see also Fig. 8). Since these fluxes were apparently dominated by the pulsed emission, we didn’t use them in the model fit. Aharonian et al. (2007a) put upper limits to the TeV gamma-ray pulsed emission of approximately one order magnitude below the total flux, and this component was excluded from the fit. The best-fit curve is shown in Fig. 5 by the solid line. The power-law index and the cutoff energy were obtained to be $\gamma_p = 2.16 \pm 0.05$ and $E_{max} = 530 \pm 399$ TeV, respectively. The total energy of high energy protons above 1 GeV, W_p , was calculated to be $W_p = 3.2 \times 10^{51} (n/1 \text{ cm}^{-3})^{-1}$ ergs, which means that the pulsar is not able to produce the TeV gamma-ray emission simply with an interstellar matter (ISM) density of 1 cm^{-3} . Dubner et al. (2002) reported a denser ISM distribution of $n \sim 10 \text{ cm}^{-3}$, derived from the HI observations with ATCA, which is indeed valid only in the northwest radio limb. If such a high density was uniformly applicable, the total energy would be reduced to $W_p = 3.2 \times 10^{50}$ ergs. Dubner et al. (2002), however, also mentioned that the southeast radio limb of the SNR showed $n \sim 0.4 \text{ cm}^{-3}$, which would yield to a higher W_p . In any case, it is revealed that the spin-down energy can not drive the acceleration of protons during its characteristic age, even if the uncertainty in the distance (see § 1) is taken into account. Therefore the hadronic gamma-ray production originated by the pulsar spin-down energy was strongly unlikely. Note that bremsstrahlung emission is not dominant in the TeV gamma-ray band under these ambient densities.

5.3. Leptonic scenario

Secondly, we discuss the leptonic scenario, and here we used a simple one-zone IC model to reproduce the multi-wavelength spectra.

Case I: The multi-band SED is plotted in Fig. 6. The

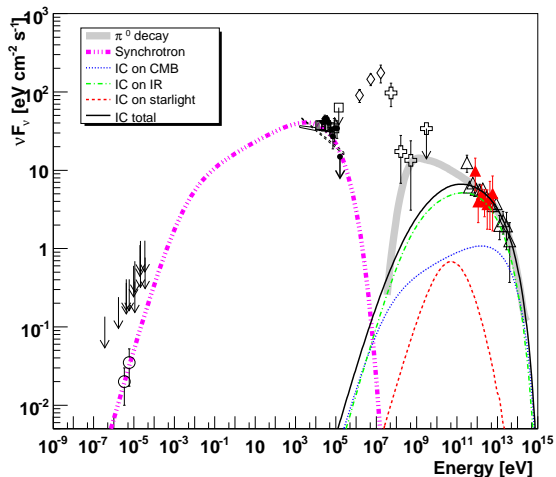


FIG. 6.— SED and leptonic model curves. The references of data are given in Table 2. Assumed electron spectrum was a broken power-law and the derived model parameters are listed in Table 3. The IC spectra on each of CMB, IR and star light are represented by dotted, dot-dashed and dashed curves, respectively. The pion decay model curve in Fig. 5 is shown by the thick curve for comparison.

data points derived from this work are represented by filled triangles and references to others are summarized in Table 2. Since *BeppoSAX*/PDS data in Mineo et al. (2001) should be corrected by the intercalibration factor of about 20% between MECS and PDS, here we plotted the corrected PDS data (Mineo 2007, private communication). The highest energy bin of the PDS represents a 1σ upper limit. IBIS measurement reported extended emission with a possible spectral cutoff at about 160 keV, at the 2.9σ confidence level from the extrapolation of the power-law spectrum. Then we present an upper limit in Fig. 6 derived from multiplying the 1σ upper limit by a factor of 3. Note that, though the data analysis of the coded-mask instrument of IBIS is ideally designed for point-like sources, Forot et al. (2006) have extracted the spectrum of the observed extended emission following a suited method developed by Renaud et al. (2006). Arrows in the radio band show the whole emission from MSH 15–52 or RCW 89 listed in du Plessis et al. (1995), which we treated as upper limits for the faint PWN. As well as in the case of the hadronic scenario, the COMPTEL and EGRET fluxes were not used as they contain a component of pulsed emission (Kuiper et al. 1999). The CMB field density on its own could not account for the TeV gamma-ray flux, and hence we added IR and optical (starlight) photon fields, following Aharonian et al. (2005). Here we used an interstellar radiation field (ISRF) derived from the latest (v50p) GALPROP package (Porter & Strong 2005; Strong & Moskalenko 2006). The ISRF is given for three components (CMB, IR from dust, and optical starlight) as a function of a distance from the Galactic center R (in kpc) and distance from the Galactic plane z (in kpc). We extracted the spectra at $(R, z) = (5.6, -0.11)$, which is shown in Fig. 7, and the nominal value is 1.4 eV/cc both for IR and optical light. The ISRF field densities did not change drastically when we considered the ambiguity in the distance, within $1.4\text{--}0.89 \text{ eV/cc}$ and $1.4\text{--}0.90 \text{ eV/cc}$ for IR and optical, respectively. Note that these values extracted from GALPROP do not represent the local densities.

The best-fit curve is shown in Fig. 6 with the assump-

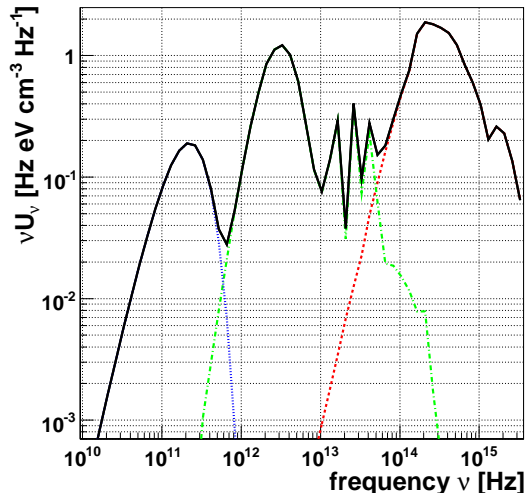


FIG. 7.— Interstellar radiation field from the GALPROP package (v50p) at $(R, z) = (5.6, -0.11)$ kpc. From lower frequencies, CMB (dotted), IR emission from interstellar dust (dot-dashed), and optical photons from stars (dashed) are shown. The solid line represents the sum of the three components.

tion of a broken power-law electron spectrum;

$$\frac{dN_e}{dE_e} \propto \frac{(E_e/E_{\text{br}})^{-\gamma_1}}{1 + (E_e/E_{\text{br}})^{(\gamma_2 - \gamma_1)}} \exp(-E_e/E_{\text{max}}) \quad (5)$$

where E_e is the electron energy, γ_1 is the spectral index of the injected electrons, γ_2 is that of the cooled electrons, and E_{br} and E_{max} are the break and maximum electron energies, respectively. The derived parameters are listed in Table 3.

Fig. 8 shows a close-up of the SED and the derived model curves. According to the IBIS measurement, the unpulsed emission is dominated by the PWN (Forot et al. 2006), which is also supported by the fact that the timing analysis showed unpulsed emission from the pulsar is indeed several factors less than the pulsed component (Cusumano et al. 2001; Forot et al. 2006). The model curve well reproduced the hard X-ray spectra. The region closed with thick solid lines in Fig. 8 represents *Chandra* measurement excluding the pulsar, which corresponds to the sum of the “diffuse PWN”, “jet” and “outer arc” fluxes listed in Delaney et al. (2006). The FOV of the *Chandra* measurement was smaller than the MECS signal region, which may cause the apparent discrepancy in the soft X-ray band. Therefore we didn’t take care of the data for the fit.

The obtained magnetic field of $17 \mu\text{G}$ was consistent with Aharonian et al. (2005), and higher than previous indications (Gaensler et al. 2002, and references therein). The IR density was also compatible with that of Aharonian et al. (2005). Although the electron index of $\gamma_1 = 1.2$ is much harder than the value of 2 predicted by general acceleration theories (e.g., Blandford & Eichler 1987), the corresponding radio spectral index of $F_\nu \propto \nu^{\alpha_r}$, $\alpha_r = -0.1$, was within typical values for PWN, $-0.3 \leq \alpha_r \leq 0$ (Weiler & Panagia 1978). The ratio of observed X-ray to gamma-ray flux showed the synchrotron cooling was dominant compared to IC cooling. Thus, the spectral break was due to the synchrotron cooling, $E_{\text{br, cool}} = 6\pi m_e^2 c^3 / (B^2 \sigma_T \tau)$, where B is a magnetic field of the PWN and σ_T is the Thomson cross section. If

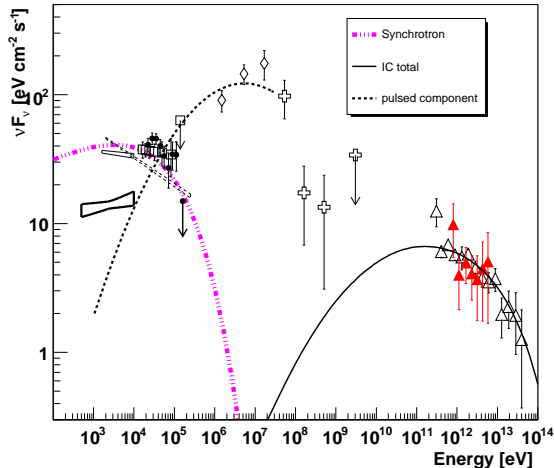


FIG. 8.— *Chandra* flux is represented by a region closed with thick lines. Other data and the synchrotron and IC model curve in Fig. 6 are also shown.

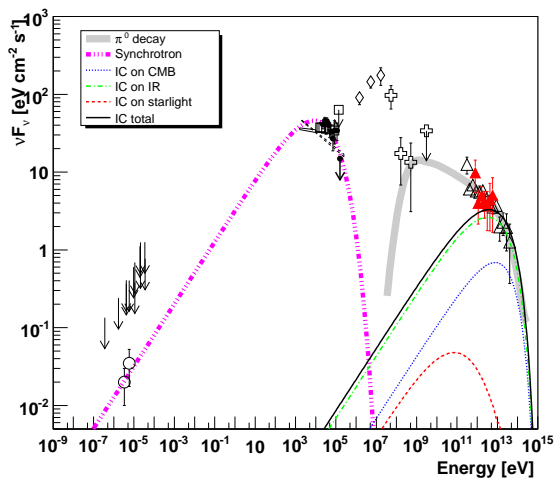


FIG. 9.— SED and the model calculation of the leptonic scenario with a single power-law electron distribution. The representation of each component is the same as in Fig. 6.

we accept a magnetic field of $17 \mu\text{G}$, the break in the photon spectrum was expected to occur at $\sim 0.2 \text{ keV}$ and $\sim 1 \text{ eV}$ for the age of $\tau = 1700 \text{ yr}$ and 20 kyr , respectively. However the electron break energy E_{br} of 77 GeV , derived from the model fit, predicts a break in the photon spectrum at lower energy of $\sim 2 \times 10^{-3} \text{ eV}$, which suggests larger B or τ . By integrating eq. (5) above 1 GeV , the total energy W_e amounts to $3.0 \times 10^{48} \text{ ergs}$. In the case of $\tau = 1700 \text{ yr}$ and $\tau_0 = 30 \text{ yr}$, $\sim 4\%$ of E_{tot} is required to be converted to W_e — an age of 20 kyr may more easily supply sufficient energy.

Case II: The expected break in the photon spectrum at $\sim 0.2 \text{ keV}$, as mentioned above, indicates that the cooling process might not be effective. Then we could alternatively apply a single power-law electron spectrum using eq. (5) with $\gamma_1 = \gamma_2$. The reproduced SED is shown in Fig. 9 with parameters in Table 3. A radio spectral index $\alpha_r = -0.6$, derived from the electron index of $\gamma_1 = \gamma_2 = 2.2$, is close to a mean value for SNRs of $\alpha_r \sim -0.5$ (e.g., Green 1991) rather than for PWNe of $-0.3 \leq \alpha_r \leq 0$. Here, the IR energy density is more than 3 times higher than that of GALPROP. There are several possible factors for variations in the local ISRF

density of this magnitude, including uncertainties in the model itself but also on the conditions in the environment of MSH 15–52. *IRAS* 15099–5856 is a candidate local source for an increased IR field, if it is associated with PSR B1509–58. IR from the surrounding dust grains were also suggested by du Plessis et al. (1995). In Fig. 9 the sub-TeV gamma-ray flux was not reproduced. If we attempt to reproduce it, the IC peak energy, which was determined by the maximum electron energy, must lie below $\sim 0.1 \text{ TeV}$. The effect of a stronger magnetic field would be to reduce the IC peaks to lower energies and also suppress the peak height. Since these IC spectra were dominated by the IR component, if the IR field density is increased, the IC peak is raised vertically in the SED. Therefore the combination of a strong magnetic field and IR radiation field, such as $B \sim 1 \text{ mG}$ and $U_{\text{IR}} \sim 7000 \text{ eV/cc}$, could reproduce the TeV gamma-ray spectra. However such a strong magnetic field would result in sufficient synchrotron cooling and cause a photon spectral break at $\sim 0.06 \text{ eV}$, in conflict with the assumption of this single power-law model. Although the requirements from energetics are looser than that of the broken power-law model, the SED is not well reproduced.

Finally, in both cases we can calculate the synchrotron and IC luminosities from the obtained model curve: $16(\text{case I})\text{--}12(\text{case II})\%$ and $0.6\text{--}0.4\%$ of the current spin-down energy $\dot{E}(\tau)$ is radiated via synchrotron emission and IC, respectively. It is also possible to estimate the equipartition magnetic field strength, B_{eq} , from the fit results as $B_{\text{eq}} = \sqrt{8\pi W_e/V}$, where V is the volume of the emission region. For Case I, if we adopt $V = 1.3 \times 10^{58} \text{ cm}^3$ in Seward et al. (1984), $B_{\text{eq}} = 76 \mu\text{G}$ is obtained, which means the PWN is particle-dominated as suggested in Chevalier (2004). Assuming V as a sphere at 5.2 kpc with $17'$ radius (corresponding to the MECS signal region), $B_{\text{eq}} = 6 \mu\text{G}$ is obtained, which is comparable with the previous indications (e.g. Gaensler et al. 2002). In this case the PWN is poynting-flux dominated. The Crab nebula is nearly in the equipartition (e.g., Atoyan 1999), while several PWNe have a deviation with a few factor from equipartition (Chevalier 2005) and for other PWNe the situation is not clear at present. As for the energetics, the total energy we have derived, W_e of $3.0 - 0.5 \times 10^{48} \text{ ergs}$ and W_p of $3.2 \times 10^{50-51} \text{ ergs}$, depend on the distance and the age of the pulsar. The uncertainty in the distance would modify the total energy by only a factor of a few, not an order of magnitude. Our estimations have been optimistic and the energetics would require a higher efficiency W_e/E_{tot} when expansion loss of PWNe is considered (Pacini & Salvati 1973; Chevalier & Fransson 1992; van der Swaluw et al. 2001; Bejger & Haensel 2003; Chevalier 2005). Although similar studies concerning the source of radiating particles have recently been started for other PWNe (eg., Funk et al. 2007,b), conclusive solutions have yet to be reached.

6. CONCLUSION

CANGAROO-III observed the SNR MSH 15-52 containing PSR B1509–58 for 48.4 hours in 2006 and detected VHE gamma-ray emission at the 7σ level. The obtained differential flux and the intrinsic extent of TeV gamma-ray emission are consistent with the previous H.E.S.S. result. Studies of the multi-wavelength spec-

tra was performed, based on both hadronic and leptonic models. In the leptonic scenario, an IR photon field and a cooled broken power-law spectrum of electrons are necessary to reproduce the TeV gamma-ray emission. From the point of view of the energetics, if we do not take into account the expansion loss, a typical supernova could provide sufficient energy for electrons to reproduce the SED, while hardly to protons. The morphology of the TeV gamma-ray emission, however, does not support the supernova explosion as the global energy source. Electrons can also be accelerated enough to reproduce the SED when $\geq 4\%$ ($\tau_0 = 30\text{yr}$ is assumed) of the rotational energy is supplied to the kinetic energy. If the pulsar was older than its characteristic age of 1700 yr, e.g., 20 kyr, the required acceleration efficiency would be reduced.

Filling in the gaps in the SED is very important for the discussion above. IR/optical measurements of the PWN emission are crucial to determine the synchrotron spectrum and the electron scenario. Additionally, the determination of the spectral break in the synchrotron or IC component would help to resolve the long-standing question of the age of this complex system. We await the results from all sky survey of the recently launched IR satellite *Akari* (Murakami et al. 2007). GLAST and the next generation of the ground-based IACTs such

as CTA (Hermann et al. 2007) and AGIS (AGIS 2007) are expected to determine the IC spectra. In addition, X-ray observations of the whole PWN, excluding PSR B1509–58, are required in order to accurately estimate the flux of synchrotron nebula emission.

The authors would like to thank Dr. T. Mineo for kindly providing us the reanalysis data of PDS. We also thank the anonymous referee for helpful comments to improve the manuscript with a careful reading. This work was supported by a Grant-in-Aid for Scientific Research by the Japan Ministry of Education, Culture, Sports, Science and Technology (MEXT), the Australian Research Council, and the Inter-University Research Program of the Institute for Cosmic Ray Research. The work is also supported by Grant-in-Aid for 21st century center of excellence programs “Center for Diversity and Universality in Physics” and “Quantum Extreme Systems and their Symmetries” of MEXT. We thank the Defense Support Center Woomera and BAE systems and acknowledge all the developers and collaborators on the GALPROP project. T. Nakamori and Y. Higashi were supported by Japan Society for the Promotion of Science Research Fellowships for Young Scientists.

REFERENCES

- AGIS 2007, http://gamma1.astro.ucla.edu/agis/index.php/Main_Page
- Aharonian, F. A., et al. 2004, *ApJ*, 614, 897
- Aharonian, F. A., et al. 2005, *A&A*, 435, L17
- Aharonian, F. A., et al. 2006, *ApJ*, 636, 777
- Aharonian, F. A., et al. 2007a, *A&A*, 466, 543
- Aharonian, F. A., et al. 2007b, *A&A*, 472, 489
- Aharonian, F. A. & Atoyan, A. M. 1986, *MNRAS*, 278, 525
- Aharonian, F. A. & Atoyan, A. M. 1998, in *Neutron Stars and Pulsars: Thirty Years after the Discovery* ed. N. Shibasaki, N. Kawai, S. Shibata & T. Kifune (Tokyo: Universal Academy Press), 439 [astro-ph/980301]
- Aharonian, F. A., Atoyan, A. M. & T. Kifune 1997, *MNRAS*, 291, 162
- Amato, E., Guetta, D. & Blasi, P. 2003, *A&A*, 402, 827
- Arendt, R. G. 1991, *AJ*, 101, 2160
- Asaoka, I. & Koyama, K. 1990, *PASJ*, 42, 625
- Atoyan, A. M. & Aharonian, F. A. 1996, *A&AS*, 120, 453
- Atoyan, A. M. 1999, *A&A*, 346, L49
- Bednarek, W. & Bartosik, M. 2003, *A&A*, 405, 689
- Bednarek, W. 2007, *Astrophys. Space Sci.*, 309, 179
- Bejger, M. & Haensel, P. 2003, *A&A*, 405, 747
- Blandford, R. D. & Eichler, D. 1987, *Phys. Rep.*, 154, 1
- Blandford, R. D. & Romani, R. W. 1988, *MNRAS*, 234, 57
- Brinkmann, W., Aschenbach, B., & Langmeier, A. 1985, *Nature*, 313, 662
- Camilo, F., Ransom, S. M., Gaensler, B. M., Slane, P. O., Lorimer, D. R., Reynolds, J., Manchester, R. N., & Murray, S. S. 2006, *ApJ*, 637, 456
- Caswell, J. L., Milne, D. K. & Wellington, K. J. 1981, *MNRAS*, 195, 89
- Chevalier, R. A. & Fransson, C. 1992, *ApJ*, 395, 540
- Chevalier, R. A. 2004, *Advances in Space Research*, 33, 456
- Chevalier, R. A. 2005, *ApJ*, 619, 839
- Cusumano, G., et al. 2001, *A&A*, 375, 397
- Delaney, T., et al. 2006, *ApJ*, 640, 929
- Dubner, G. M., et al. 2002, *AJ*, 123, 337
- du Plessis, I., et al. 1995, *ApJ*, 453, 746
- Enomoto, R., et al. 2002, *Astropart. Phys.* 16, 235
- Enomoto, R., et al. 2006, *ApJ*, 638, 397
- Fisher, R. A. 1936, *Annals of Eugenics*, 7, 179
- Forot, M., Hermsen, W., Renaud, M., Laurent, P., Grenier, I., Goret, P., Khelifi, B., & Kuiper, L. 2006, *ApJ*, 651, L45
- Funk, S., et al. 2007, *A&A*, 470, 249
- Funk, S., Hinton, J. A., Pühlhofer, G., Aharonian, F. A., Hofmann, W., Reimer, O., Wagner, S. 2007, *ApJ*, 662, 517
- Gaensler, B. M., Brazier, K. T. S., Manchester, R. N., Johnston, S., & Green, A. J. 1999, *MNRAS*, 305, 724
- Gaensler, B. M., Arons, J., Kaspi, V. M., Pivovarov, M. J., Kawai, N., & Tamura, K. 2002, *ApJ*, 569, 878
- Gaensler, B. M. & Slane, P. O. 2006, *ARA&A*, 44, 17
- Gelfand, J. D., et al. 2007, *ApJ*, 663, 468
- Green, D. A. 1991, *PASP*, 103, 209
- Gunji, S., et al. 1994, *ApJ*, 428, 284
- Gvaramadze, V. V. 2001, *A&A*, 374, 259,
- Harding, A. K. 1996, *Space Sci. Rev.*, 75, 257
- Helfand, D. J., Gotthelf, E. V., & Halpern, J. P. 2001, *ApJ*, 556, 380
- Hermann, G., et al. 2007, *Proc. 30th ICRC (Merida)*, 196 (arXiv:0709.2048)
- Hillas, A. M. 1985, *Proc. 19th ICRC (La Jolla)*, 3, 445
- Hinton, J. & Aharonian F. A. 2007, *ApJ*, 657, 302
- Hinton, J. 2007, *Proc. 30th ICRC (Merida)*, 1335
- Hoppe, S. 2007, *Proc. 30th ICRC (Merida)*, 269
- Horns, D. 2006, *A&A*, 451, L51
- Horns, D. et al. 2007, *Astrophys. Space Sci.*, 309, 189
- Kabuki, S., et al. 2003, *Nucl. Inst. Meth.*, A500, 318
- Kabuki, S., et al. 2007, *ApJ*, in press[arXiv.0706.0367]
- Kaplan, D. L., & Moon, D. 2006, *ApJ*, 644, 1056
- Kaspi, V. M., Manchester, R. N., Siegman, B., Johnston, S., & Lyne, A. G. 1994, *ApJ*, 422, L83
- Kawachi, A., et al. 2001, *Astropart. Phys.*, 14, 261
- Kawai, N., Okayasu, R., & Sekimoto, Y. 1993, *Proc. AIP Conf.* 280, p.213
- Khelifi, B., et al. 2005, *Proc. 29th ICRC (Pune)*, 4, 127
- Kubo, H., et al. 2003, *Proc. 28th ICRC (Tsukuba)*, 2863
- Kuiper, L., Hermsen, W., Krijger, J. M., Bennett, K., Carramiñana, A., Schönfelder, V., Bailes, M., & Manchester, R. N. 1999, *A&A*, 351, 119
- Livingstone, M. A., Kaspi, V. M., Gavriil, F. P., & Manchester, R. N. 2005, *ApJ*, 619, 1046
- Lyne, A. G., Pritchard, R. S., & Smith, F. G. 1988, *MNRAS*, 233, 667
- Manchester, R. N., Tuohy, I. R., & D’Amico, N. 1982, *ApJ*, 262, L31
- Marsden, D., et al. 1997, *ApJ*, 491, L39
- Matz, S. M., et al. 1994, *ApJ*, 434, 288

TABLE 2
SUMMARY OF DATA USED IN THE SED ANALYSIS.

Detector	Marker	Pulse component	Spatial component ^a	Reference
ATCA	open circle	unpulsed	N	(1)(2)
<i>Chandra</i> /ACIS	closed region(thick lines)	pulsed+unpulsed	NJ	(2)(3)
SAX/MECS	closed region(thin lines)	unpulsed	PNJRC	(4)
SAX/PDS	open square	unpulsed	PNJRCO	(5)
<i>INTEGRAL</i> /IBIS	filled circle	unpulsed	PNJRC	(6)
<i>RXTE</i> /PCA+HEXTE	closed region(dotted lines)	unpulsed	PNJRCO	(7)
COMPTEL	open diamond	pulsed+unpulsed	PNJRCO	(8)
EGRET	open cross	pulsed+unpulsed	PNJRCO	(8)
H.E.S.S.	open triangle	pulsed+unpulsed	PNJRC	(9)
CANGAROO-III	filled triangle	pulsed+unpulsed	PNJRC	this work

REFERENCES. — (1) Gaensler et al. 1999; (2) Gaensler et al. 2002; (3) Delaney et al. 2006; (4) Mineo et al. 2001; (5) Mineo 2007, private communication (6) Forot et al. 2006; (7) Marsden et al. 1997; (8) Kuiper et al. 1999; (9) Aharonian et al. 2005;

^a N: Diffuse PWN defined in ref (2), J: Jet and outer arc defined in ref (2) and (3), P: Pulsar, C: Central Diffuse Nebula defined in Trussoni et al. (1996), R: RCW89, O: Outside MSH 15–52

TABLE 3
SUMMARY OF PARAMETERS USED IN LEPTONIC MODEL.

Electron spectrum	B [μ G]	γ_1	γ_2	E_{br} [GeV]	E_{max} [TeV]	U_{IR} [eV/cc]	W_e [ergs]	L_{sync}^a [ergs/s]	L_{IC}^b [ergs/s]
broken P.L.	17	1.2	2.7	77	2.5×10^2	2.3	3.0×10^{48}	2.9×10^{36}	1.2×10^{35}
single P.L.	20	2.2	2.2	-	1.3×10^2	4.5	5.4×10^{47}	2.1×10^{36}	7.7×10^{34}

^a Luminosity of synchrotron emission calculated from the model fit curve.

^b Luminosity of inverse Compton emission calculated from the model fit curve.

- Mineo, T., Cusumano, G., Maccarone, M. C., Massaglia, S., Massaro, E., & Trussoni, E. 2001, *A&A*, 380, 695
Murakami et al., 2007, *PASJ*, in press (arXiv: 0708.1796)
Nishijima, K., et al. 2005, *Proc. 29th ICRC (Pune)*, 15, 327
Nomoto, K., Mazzali, P. A., Nakamura, T., Iwamoto, K., Danziger, I. J., & Patat, F. 2001, in *Supernovae and Gamma-Ray Bursts: The Greatest Explosions Since the Big Bang*, ed. M. Livio, N. Panagia, & K. Sahu (Cambridge: CUP), 144 [astro-ph/0003077]
Pacini, F. & Salvati, M. 1973, *ApJ*, 186, 249
Porter, T. A. & Strong, A. W., 2005, *Proc. 29th ICRC (Pune)*, 00, 101
Renaud, M., Gros, A., Lebrun, F., Terrier, R. Goldwurm, A., Reynolds, S., & Kakemci, E. 2006, *A&A*, 456, 389
Rodgers, A. W., Campbell, C. T., & Whiteoak, J. B. 1960, *MNRAS*, 121, 103
Saito, Y., Kawai, N., Kamae, T. et al. 1997, *Proc. AIP Conf.*, 410, p.628
Sako, T., et al. 2000, *ApJ*, 537, 422
Seward, F. D. & Harden, F. R. 1982, *ApJ*, 256, L45
Seward, F. D., Harnden, F. R., Jr., Murdin, P., & Clark, D. H. 1983, *ApJ*, 267, 698
Seward, F. D., Harnden, F. R., Jr., Szymkowiak, A., & Swank, J. 1984, *ApJ*, 281, 650
Shearer, A., O’Sullivan, C. M. M., Golden, A., Garcia, P. V. R., Redfern, M., Danks, A., & Cullum, M. 1998, *A&A*, 333, L16
Strong, W. S. & Moskalenko, I. V. 2006, GALPROP project, http://galprop.stanford.edu/web_galprop/galprop_home.html
Tamura, K., Kawai, N., Yoshida, A., & Brinkmann, W. 1996, *PASJ*, 48, L33
Taylor, J., H. & Cordes, J. M. 1993, *ApJ*, 411, 674
Thompson, D. J. 2003, *Cosmic Gamma Ray Sources*[astro-ph/0312272]
Trussoni, E., Brinkmann, W., Ogelman, H., Hasinger, G., Aschenbach, B., & Ferrari, A. 1990, *A&A*, 234, 403
Trussoni, E., Massaglia, S., Caucino, S., Brinkmann, W., & Aschenbach, B. 1996, *A&A*, 306, 581
Van den Bergh, S. & Kramper, K. W. 1984, *ApJ*, 280, L51
van der Swaluw, E., Achterberg, A., Gallant, Y. A. & Tóth, G. 2001, *A&A*, 380, 309
Weiler, K. W., & Panagia, N. 1978, *A&A*, 70, 419
Yatsu, Y., et al. 2005, *ApJ*, 631, 312